Ultrasound in Med. & Biol., Vol. 33, No. 12, pp. 1841–1858, 2007

0301-5629/07/$–see front matter

ELSEVIER

doi:10.1016/j.ultrasmedbio.2007.05.020

● *Original Contribution*

NONINVASIVE VASCULAR ELASTOGRAPHY: TOWARD A COMPLEMENTARY CHARACTERIZATION TOOL OF ATHEROSCLEROSIS IN CAROTID ARTERIES

CÉDRIC SCHMITT,* GILLES SOULEZ,† ROCH L. MAURICE,* MARIE-FRANCE GIROUX,† and GUY CLOUTIER*

*Laboratory of Biorheology and Medical Ultrasonics, University of Montreal Hospital Research Center; and †Department of Radiology, University of Montreal Hospital, Montreal, Quebec, Canada

(*Received* 4 *October* 2006, *revised* 25 *May* 2007, *in final form* 30 *May* 2007)

Abstract—Only a minority of patients with carotid arterial disease have warning symptoms, because the majority of strokes are caused by previously asymptomatic lesions. Because morbidity and mortality after acute stroke are high, patients should be diagnosed and treated before symptoms develop. The hypothesis of this study is that vascular elasticity maps (or elastograms) of carotids are of predictive value for plaque characterization. The strain tensor from either cross-sectional or longitudinal ultrasound radiofrequency data were assessed by a new implementation of the Lagrangian speckle model estimator (LSME), which considers local echogenicity variations. A 26-year-old healthy male (HS1), a 40-year-old (HS2) normal female subject and two 75-year-old asymptomatic patients with severe carotid stenoses were scanned. Reproducible elastograms were obtained as a function of time over five to seven cardiac cycles. Stress-strain modulus elastograms were computed for normal subjects. Stiffening of healthy carotid walls was estimated to be 148 ± 7 kPa and 163 ± 30 kPa at peak-systole for HS1 and HS2, respectively. For patients with heterogeneous plaques, strain and shear elastograms revealed interesting information about plaque size, tissue composition and mechanical interaction between structures. In conclusion, the LSME provides a promising approach for strain and shear estimates to characterize vulnerable plaque. (E-mail: guy.cloutier@umontreal.ca) **© 2007 World Federation for Ultrasound in Medicine & Biology.**

Key Words **Noninvasive vascular ultrasound elastography, Vascular pathology, Ultrasound imaging, *In vivo* elasticity imaging, Carotid stenoses, Stroke.**

INTRODUCTION

Stroke is the third leading antecedent of death and the greatest cause of morbidity (Thom et al. 2006). Its main etiology (70–80%) is atherosclerosis leading to cerebral emboli or thrombosis. More than 60% of all cerebral infarctions are evoked by rupture of a vulnerable plaque (Casscells et al. 2003). Among individuals with carotid bifurcation disease, only a minority have warning symptoms, the majority experiencing a stroke from previously asymptomatic lesions (Nicolaides et al. 2003). Carotid endarterectomy is an established effective therapy for secondary prevention of stroke in patients with symptomatic carotid stenosis (>70%) (NASCET 1991; ECST 1998). On the other hand, preventive carotid endarterectomy for asymptomatic stenosis is of marginal benefit (Chaturvedi 1999; Connors et al. 2000). Hence, additional diagnostic tools need to be developed to identify patients at risk.

Vulnerable carotid plaque usually consists of a thin fibrous cap, a large lipid core and dense macrophage inflammation on or beneath its surface (Naghavi et al. 2003; Faxon et al. 2004). Calcified plaques are significantly less likely to be symptomatic than noncalcified plaques and are therefore probably more stable (Nandalur et al. 2005). Intraplaque hemorrhage (IH) has been linked as a potential factor in plaque vulnerability of coronary arteries (Kolodgie et al. 2003). For carotid arteries, the results are conflicting, with some studies showing an association between the

Address correspondence to: Guy Cloutier, University of Montreal Hospital Research Center, Laboratory of Biorheology and Medical Ultrasonics, 2099 Alexandre de Seve, room Y-1619, Montreal, Quebec, H2L 2W5 Canada. E-mail: guy.cloutier@umontreal.ca

presence of symptoms and IH (Imparato et al. 1983; Takaya et al. 2005), and others showing no association (Montauban van Swijndregt et al. 1999).

In this context, it is recognized that the mechanical properties of plaques should be of predictive values (Reneman et al. 2005). To follow modifications in arterial wall mechanical properties, numerous parameters have been proposed (*e.g.*, arterial distensibility, compliance, stiffness index; Lehmann 1999; O'Rourke et al. 2002). The underlying theory supporting these indices is Hooke's law. The main assumption of this law is that arteries have an axisymmetrical geometry. In the presence of plaques, arterial wall morphology and internal composition become heterogenous. Previous techniques have significant drawbacks for the quantification of these complex geometries. As a possible solution to such limitations, current methods study plaque motion and strain under pulsating physiological conditions. Meairs and Hennerici (1999) designed a system to reconstruct the 4-D motion of plaques. They developed an algorithm based on optic flow equations. This method demonstrated possible discrimination in plaques of symptomatic and asymptomatic patients.

Other algorithms assess local wall motions from B-mode (Golemati et al. 2003) or radiofrequency (RF) mode images (Bang et al. 2003; Dahl et al. 2004). The Dahl et al. (2004) study of six asymptomatic and six symptomatic patients showed that only a few (*e.g.*, time average of mean velocity amplitude over plaque, minimum in time of mean velocity curl over plaque) among 29 motion parameters provided reproducible estimations (Dahl et al. 2004). Kanai et al. (2003) proposed a method that tracks the motion of different vascular layers *via* demodulated RF phase and amplitude signals. Young's modulus distributions were reconstructed by assuming incompressible and isotropic medium subjected to stress, which decrease linearly from the center of the lumen to the intima.

Recently, we proposed a new method to noninvasively assess the elasticity of vascular walls (Maurice et al. 2004; Schmitt 2005). With the Lagrangian speckle model estimator (LSME), noninvasive vascular elastography (NIVE) directly provides axial and lateral strain and shear estimations without the requirement of computing derivative of the displacement field (Maurice et al. 2004). In this paper, a new formulation of the LSME was implemented. To counteract possible decorrelation noise because of speckle intensity variations after tissue deformation, two parameters that compensate for these artefacts were incorporated in our model. The formulation was inspired by an image registration algorithm (Periaswamy and Farid 2003) that considers local image intensity variations and is adapted to NIVE to assess 2-D elastograms.

MATERIALS AND METHODS

Radiofrequency data processing

Strain and shear estimations. As stated by Maurice et al. (2004), tissue motion estimation requires subdividing the region-of-interest (ROI) into small measurement windows (MWs) within which tissue motion is assumed affine. To compute such affine transformations between two RF images, we adapted the LSME (Maurice et al. 2004) to the formulation introduced by Periaswamy and Farid (2003). In the general model of Periaswamy and Farid (2003), two parameters are modeling cases for which the assumption of brightness constancy between premotion and postmotion images fails. In ultrasound (US) imaging, this intensity variation is known as decorrelation noise produced by speckle motion artefacts, out-of-plane motion, nonuniform motion, subresolution scatterers, nonuniformity of the ultrasound field, nonrigid tissue deformation, *etc.* (Yeung et al. 1998; Maurice and Bertrand 1999), and it is at the origin of numerous incorrect estimations. Additional to the LSME, our new model takes into account linear intensity variations.

By denoting (x_t, y_t) and (x_{t-1}, y_{t-1}) as postmotion and premotion pixel coordinates, affine transformation is modeled as:

$$\begin{bmatrix} x_t \\ y_t \end{bmatrix} = LT \begin{bmatrix} x_{t-1} \\ y_{t-1} \end{bmatrix} + TR \tag{1}$$

with

$$LT \begin{bmatrix} \Delta_{xx} & \Delta_{xy} \\ \Delta_{yx} & \Delta_{yy} \end{bmatrix} \tag{2}$$

and

$$TR = \begin{bmatrix} d_x \\ d_y \end{bmatrix}, \tag{3}$$

where LT and TR are the linear transformation matrix and translation vector, respectively. The LT matrix contains two terms denoting axial $(1-\Delta_{yy})$ and lateral $(1-\Delta_{xx})$ compression/dilation and two terms describing axial (Δ_{yx}) and lateral (Δ_{xy}) shears, whereas TR represents axial (d_y) and lateral (d_x) translations. Within a MW, premotion and postmotion RF data images can be written as:

$$I(x,\ y,\ t) = I(\Delta_{xx}x + \Delta_{xy}y + d_x,\ \Delta_{yx}x + \Delta_{yy}y + d_y,\ t-1). \tag{4}$$

To account for possible intensity variations between images, two new parameters are incorporated into the previous formulation, λ and γ, defined as contrast and

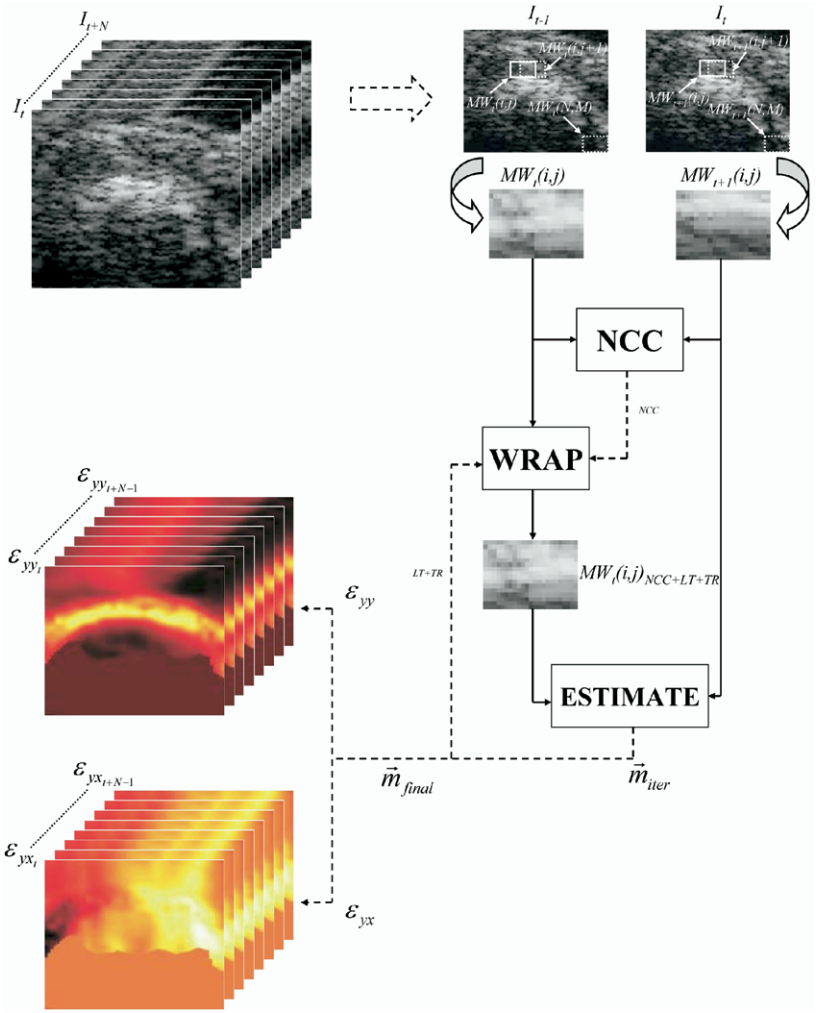

Fig. 1. Block diagram of algorithm implementation assessing axial strain (ϵ_{yy}) and shear (ϵ_{yx}) for one measurement window (MW) before ($MW_t(i,j)$) and after ($MW_{t+1}(i,j)$) motion.

brightness, respectively. By adding these parameters to eqn (4), the model becomes:

$$\lambda I(x,\ y,\ t) + \gamma = I(\Delta_{xx}x + \Delta_{xy}y + d_x,\ \Delta_{yx}x + \Delta_{yy}y + d_y,\ t-1). \quad (5)$$

The goal of this estimator is to assess the optimal value of vector $\vec{m}$ (eqn (6)) that verifies eqn (5). One method consists of minimizing the mean square errors between premotion and postmotion images. This minimization problem is solved for each MW.

$$E_{MW}(\vec{m}) = \sum_{x,\ y \in MW} [\lambda I(x,\ y,\ t) + \gamma - I(\Delta_{xx}x + \Delta_{xy}y + d_x,\ \Delta_{yx}x + \Delta_{yy}y + d_y,\ t-1)]^2, \quad (6)$$

with:

$$\vec{m}_{MW} = [\Delta_{xx},\ \Delta_{xy},\ \Delta_{yx},\ \Delta_{yy},\ d_x,\ d_y,\ \lambda,\ \gamma]. \quad (7)$$

However, eqn (6) is nonlinear in its unknowns. It is then linearized by first-order truncated Taylor series expansion to become:

$$E_{MW}(\vec{m}) = \sum_{x,\ y \in MW} [\lambda I(x,\ y,\ t) + \gamma - I(x,\ y,\ t) + I_t(x,\ y,\ t) - (\Delta_{xx}x + \Delta_{xy}y + d_x)I_x(x,\ y,\ t) - (\Delta_{yx}x + \Delta_{yy}y + d_y)I_y(x,\ y,\ t)]^2, \quad (8)$$

where $I_x(.) = \dfrac{\partial I}{\partial x}$, $I_y(.) = \dfrac{\partial I}{\partial y}$ and $I_t(.) = \dfrac{\partial I}{\partial t}$ are spatio-temporal partial derivatives.

The previous equation can be rewritten in vector form as:

$$E_{MW}(\vec{m}) = \sum_{x,\,y\in MW}\left[\underbrace{(I_t - I + xI_x + yI_y)}_{k} - \underbrace{(xI_x\ \ yI_x\ \ I_x\ \ xI_y\ \ yI_y\ \ I_y\ I\ \ 1)}_{\vec{c}}\left(\underbrace{\Delta_{xx}\ \ \Delta_{xy}\ \ d_x\ \ \Delta_{yx}\ \ \Delta_{yy}\ \ d_y\ \ \lambda\ \gamma}_{\vec{m}}\right)^T\right]^2 = \sum_{x,\,y\in MW}[k - \vec{c}\vec{m}^T]^2 \quad (9)$$

From eqn (9), the error function $E_{MW}(\vec{m})$ can be minimized analytically by differentiating with respect to the unknown $\vec{m}$, *i.e.*,

$$\frac{dE_{MW}(\vec{m})}{d\vec{m}} = \sum_{x,\,y\in MW} -2\vec{c}[k - \vec{c}\vec{m}^T]. \quad (10)$$

Finally, $\vec{m}$ is calculated when the energy derivative is equal to zero:

$$\frac{dE_{MW}(\vec{m})}{d\vec{m}} = 0, \vec{m} = \left[\sum_{x,\,y\in MW}\vec{c}\vec{c}^T\right]^{-1}\left[\sum_{x,\,y\in MW}\vec{c}k\right]. \quad (11)$$

The deformation matrix (DM or Δ) is related to the strain tensor (ε) as:

$$\varepsilon_{ij} = \frac{1}{2}[\Delta_{ij} + \Delta_{ji}]. \quad (12)$$

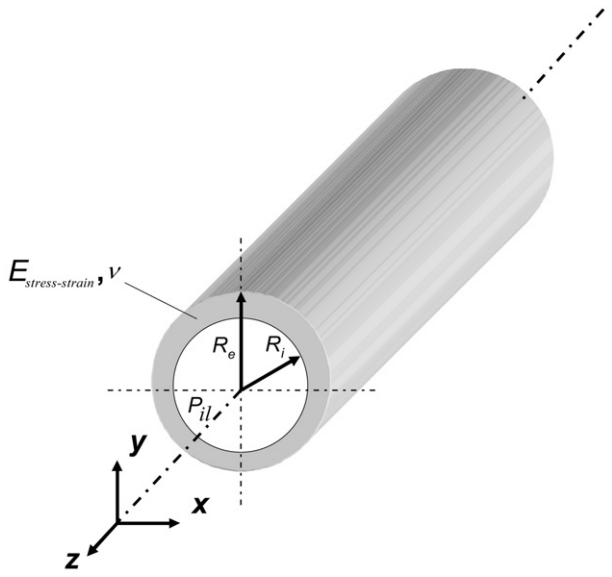

Fig. 2. Geometry of an axisymmetrical, hollow cylinder with inner and outer radius R_i and R_o, respectively. Intraluminal pressure gradient P_{il} induces wall deformation, defined by a stress-strain modulus $E_{stress\text{-}strain}$ and Poisson coefficient ν.

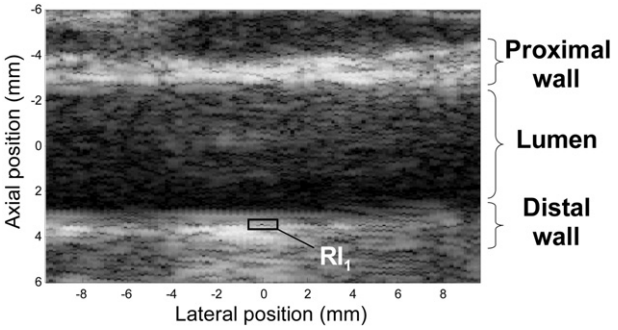

Fig. 3. Longitudinal B-mode image of a 26-year-old healthy man's distal common carotid artery. The small window RI_1 is defined in the distal wall.

In practical terms, the method is implemented by MATLAB 7.0 (The MathWorks, Inc., Natick, MA, USA) and takes a maximum of 5 min to compute one elastogram on a personal computer (AMD Athlon 64*2 Dual Core processor, 2.2 GHz, 2 GB of memory). As summarized in Fig. 1, it is implemented in three steps, and it is conceivable to use parallelization to speed up computations:

1. Premotion and postmotion RF images are subdivided into small windows (or MW) defined by size and overlap.
2. For each MW, a registration in translation is done according to a 2-D normalized cross-correlation technique. This method has shown good accuracy in similar applications (Langeland et al. 2003).
3. Then, until the last iteration is not reached, vector $\vec{m}$ is assessed with eqn (11), and the image previously registered in translation is wrapped according to the DM. $\vec{m}$ parameters at the last iteration are the ones that are taken to build ε_{yy} and ε_{yx} 2-D distributions.

Elastic modulus calculation

To calculate an elastic modulus for healthy vessels (axisymmetrical and homogenous vascular wall common carotids), an inverse problem based on an analytical formulation was tested (Maurice et al. 2004). Given a hollow, thick-wall cylinder characterized by R_i, R_o, $E_{stress\text{-}strain}$ and P_{il} as the inner and outer radius, stress-strain modulus distribution and intraluminal pressure gradient, respectively (Fig. 2), axial strain parameters were defined as:

$$\varepsilon_{yy}(x,\ y) = K_\infty\frac{x^2 - y^2}{(x^2 + y^2)^2}, \quad (13)$$

$$K_\infty = \frac{3}{2}P_{il}\left[E_{stress-strain}\left(\frac{1}{R_i^{\,2}} - \frac{1}{R_0^{\,2}}\right)\right]^{-1}. \quad (14)$$

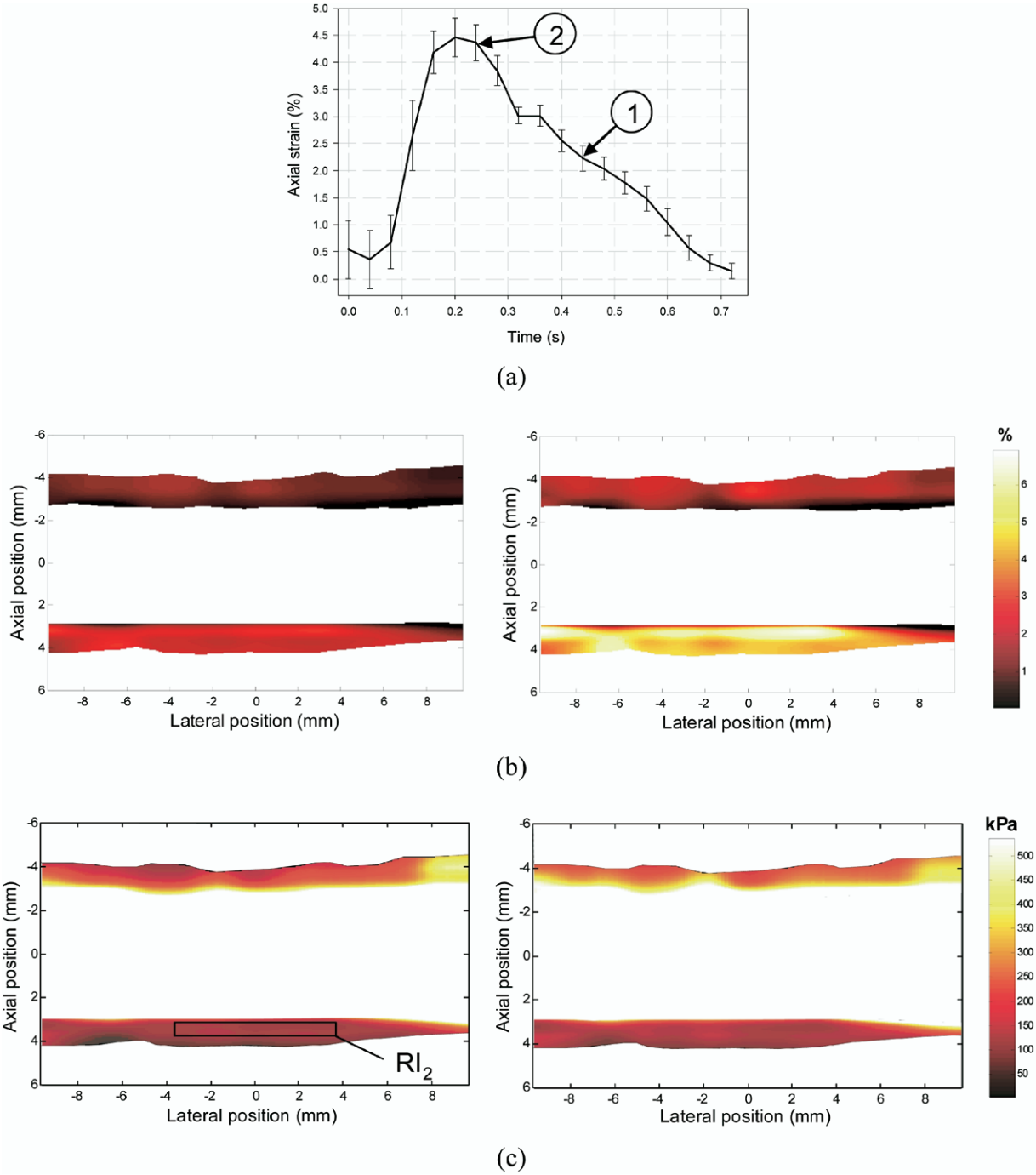

Fig. 4. Axial deformation calculated in windows defined by RI_1 (Fig. 3) averaged on five consecutive cardiac cycles (a). Two-dimensional axial strain of the distal and proximal carotid artery wall loaded with a pressure gradient of 18.5 mm Hg (①) (b, left panel) or 37 mm Hg (②) (b, right panel). Two-dimensional stress-strain modulus for a pressure gradient equal to 18.5 mm Hg (c, left panel) and 37 mm Hg (c, right panel). RI_2 is defined in the distal wall. The lumen is segmented in white.

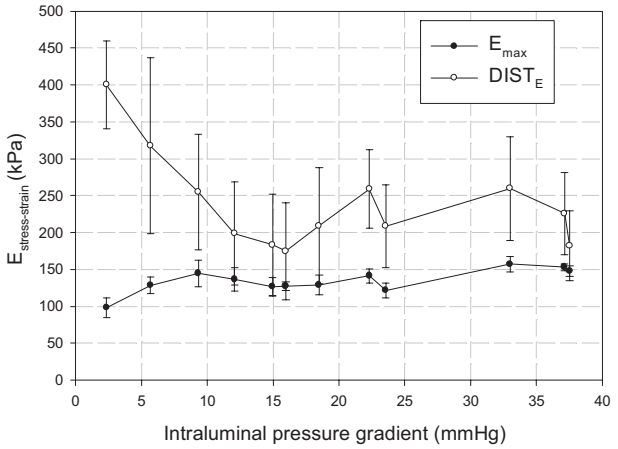

Fig. 5. E_{max} and $DIST_E$ of the whole distal wall as a function of the intraluminal pressure gradient (ranging from 2.3–37.5 mm Hg) by using the 1-D inverse problem solution from longitudinal acquisition and for five cardiac cycles.

With our method, we acquired longitudinal images and assumed that the probe was located at the center of the vessel ($x = 0$ mm), perpendicular to blood flow. From eqns (13) and (14), $E_{stress\text{-}strain}$ is given as:

$$E_{stress-strain}(x,\ y) = \frac{3}{2}\cdot\frac{P_{il}}{\left(\frac{1}{R_i^{\,2}}-\frac{1}{R_0^{\,2}}\right)}\cdot\left.\frac{x^2-y^2}{\varepsilon_{yy}(x,\ y)\cdot(x^2+\ y^2)^2}\right|_{x=0}, \quad (15)$$

or

$$\left|E_{stress-strain}(0,\ y)\right| = \frac{3}{2}\cdot\frac{P_{il}}{\left(\frac{1}{R_i^{\,2}}-\frac{1}{R_0^{\,2}}\right)}\cdot\frac{1}{\varepsilon_{yy}(0,\ y)\cdot\ y^2}. \quad (16)$$

Two-dimensional elastic modulus reconstruction simply consisted of assessing the axial strain $\varepsilon_{yy}(0,y)$ for each position in the z-direction, and calculating $E_{stress\text{-}strain}$ with eqn (16).

From 2-D stress-strain modulus distribution, as proposed previously by Kanai et al. (2003), elasticity histogram distribution was used as a quantitative description. Two new parameters were introduced here as descriptive indices, which denote predominant stiffness (E_{max}) and dispersion ($DIST_E$). E_{max} was defined as the highest peak (highest occurrence) on the stress-strain modulus histogram, whereas $DIST_E$ was the mean deviation computed as:

$$DIST_E = \frac{1}{Q}\sum_i [abs(E_{\max} - E_i)], \quad (17)$$

with Q being the number of bins in the histogram, and E_i the occurrence of bin i.

Study population

The study comprised four subjects: one healthy 26-year-old man (HS1), one 40-year-old healthy woman (HS2), one 75-year-old male with asymptomatic carotid stenosis diagnosed by previous Doppler US and computed tomography angiography (CTA) examinations (PAS1, 90% stenosis) and one 75-year-old male with atherosclerotic calcified wall (PAS2). All subjects gave their informed consent for examination and the protocol was approved by the Ethics Committee of the CHUM Research Centre.

Ultrasound image acquisition and protocol

High-quality B-mode and echo-Doppler images were acquired with a Philips 5000 system (Philips Medical Systems, Bothell, WA, USA), whereas RF data, not available on the Philips instrument, were recorded with an Ultrasonix RP550 scanner (Ultrasonix Medical Corporation, Burnaby, BC, Canada). Each person lay supine during the clinical examination. For RF image acquisition, the ultrasonic scanner was configured with a frame rate ranging from 19 to 25 images/s. Such a frame rate is sufficient for this particular application because, as opposed to the method of Bang et al. (2003), our estimator recovers the deformation matrix that is valid for relatively large local displacements. The window width of the US scanner was reduced from 38 mm to 19 mm to allow such a frame rate, and depth was adjusted to match the ROI. The excitation frequency of the L14–

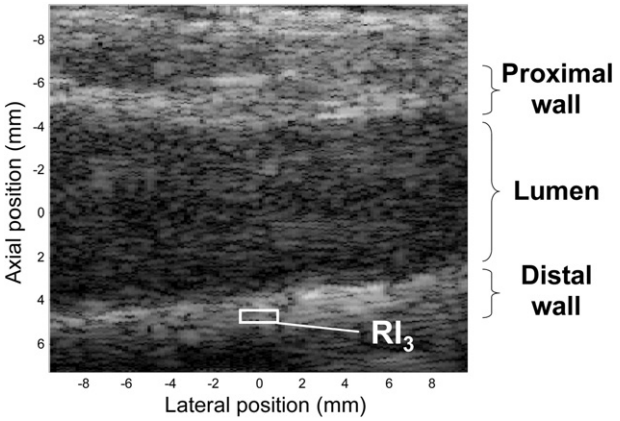

Fig. 6. Longitudinal B-mode image of a 40-year-old healthy woman's distal common carotid artery. The proximal wall, lumen and distal wall are identified. The small window RI_3 is defined in the distal wall.

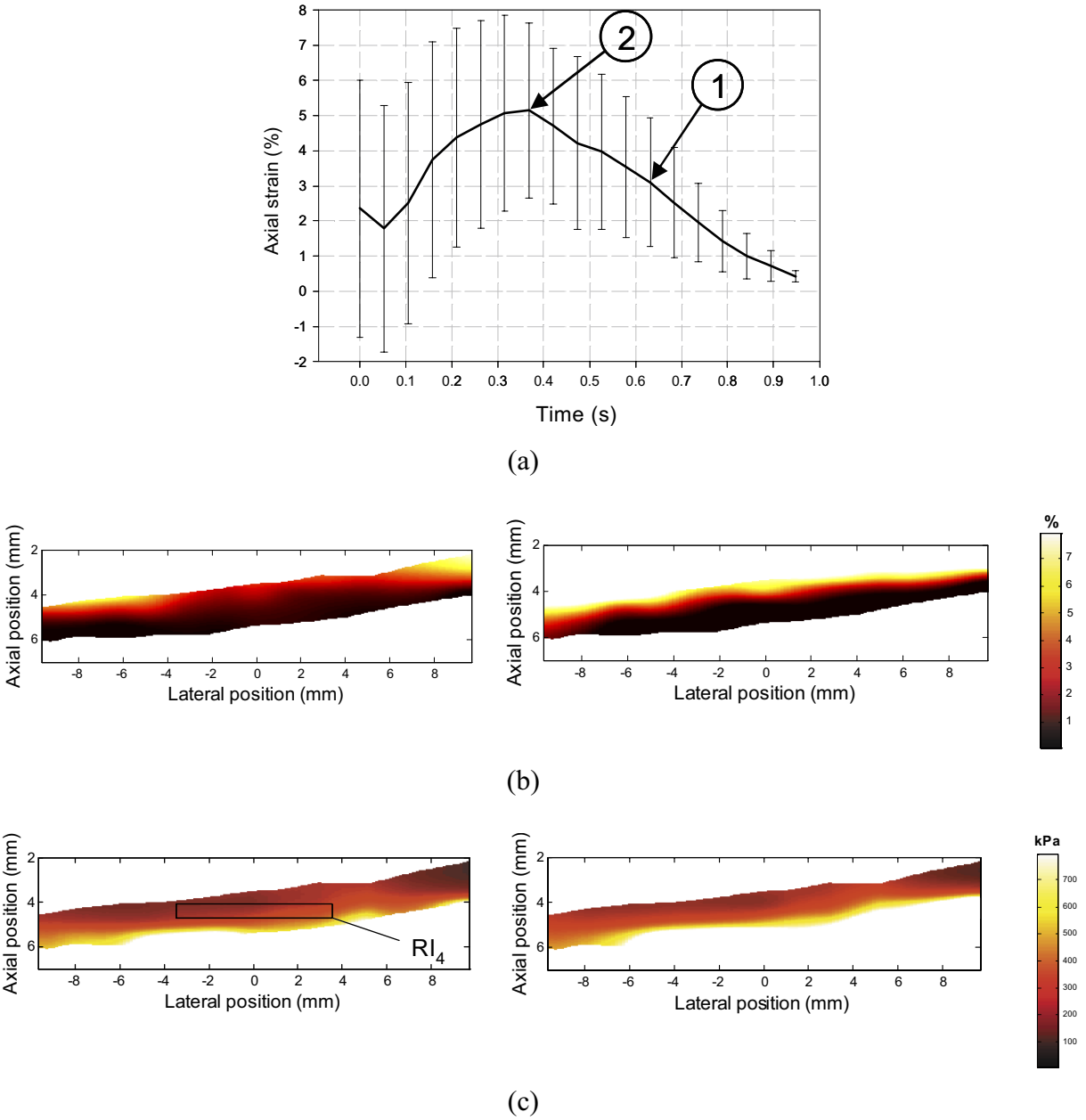

Fig. 7. Axial deformation calculated in windows defined by RI_3 (Fig. 6) average on five consecutive cardiac cycles (a). Two-dimensional axial strain of the distal carotid artery wall loaded with a pressure gradient of 30.4 mm Hg (①) (b, left panel) or 47 mm Hg (②) (b, right panel). Two-dimensional stress-strain modulus for a pressure gradient equal to 30.4 mm Hg (c, left panel) or 47 mm Hg (c, right panel). RI_4 is defined in the distal wall. The lumen is segmented in white.

5/38 probe (Ultrasonix) and sampling frequency were 10 MHz and 40 MHz, respectively.

During this protocol, cross-sectional and longitudinal color Doppler images and RF data were recorded in the distal common and proximal and distal internal carotid arteries. Arterial diastolic and systolic pressures were measured with a brachial cuff, before and after image acquisition. Moreover, electrocardiograms (ECGs) were taken for postprocessing synchronization. For patients with carotid atherosclerosis, RF images were recorded within maximum stenosis (PAS1) and at the site of calcification deposit (PAS2).

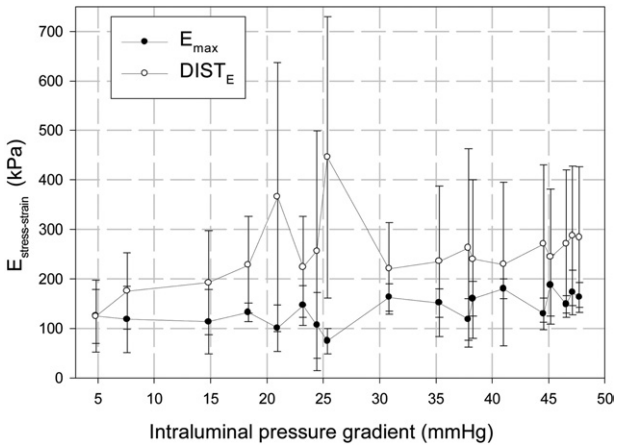

Fig. 8. E_{max} and $DIST_E$ of the whole distal wall as a function of the intraluminal pressure gradient (ranging from 4.8–47 mm Hg) by using the 1-D inverse problem solution from longitudinal acquisition and for five cardiac cycles.

Image segmentation and consideration of pressure values

In healthy subjects, the outer common carotid artery interface (outer adventitia) was difficult to detect. This could induce incorrect segmentations of the vessel wall. Moreover, artefactual multiple reflection echoes (as a result of hyperechogenic regions) were often observed in the lumen. Consequently, a semiautomatic segmentation method is proposed to localize the arterial wall. Segmentation was performed in four steps:

1. Manual inner lumen segmentation in end-diastole.
2. By considering carotid artery wall thickness (intima, media and adventitia) in end-diastole, as reported in the literature (Kazmierski et al. 2004), automatic segmentation was performed to find the outer artery boundary.
3. Manual inner lumen segmentation in peak-systole.
4. By assuming parietal deformation as being proportional to lumen diameter, wall thickness was calculated from peak-systole reduced by the axial strain value assessed by our estimator. This technique recovered the inner and outer vessel diameters for each image within the cardiac cycle.

Finally, arterial systolic and diastolic pressure values were integrated into the lumen diameter plots as maximal and minimal pressures, respectively. This technique assumes a similar waveform between local strain estimation and intraluminal pressure. The underlying assumption is based on the mechanical behavior of large elastic arteries (Segers et al. 2004). Indeed, in this case, inner wall motion can serve as an intraluminal pressure substitution parameter. The displacement vector being directly linked to strain with a derivation operator, our method allows us to recover instantaneous blood pressure. This postprocessing was essential to estimate all parameters needed for computing the elastic modulus defined in eqn (16), at each instant in the cardiac cycle.

Table 1. Parameters used for RF signal pre-processing and estimator configurations.

	Interpolation factor		Windows size (mm)		Overlapping (%)	
	Axial	Lateral	Axial	Lateral	Axial	Lateral
HS1, HS2	1	1	2.89	5.98	80	80
PAS1					80	80
Cross-sectional	2	4	1.44	1.5	80	80
Longitudinal	2	4	1.92	2.24	80	80
PAS2	2	4	0.77	1.11	85	85

For the two diseased arteries, another method was used to segment the arterial wall. Indeed, in these cases, image quality was degraded by the presence of large calcified regions around the lumen (shadowing artefact). This problem was counteracted by segmentation with the aid of color Doppler and computed tomography (CT) images. Two regions were arbitrarily segmented manually: calcified plaque (CP),

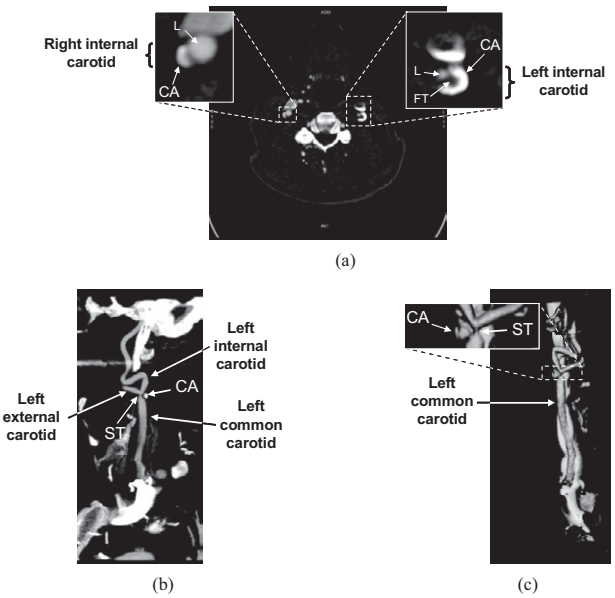

Fig. 9. (a) Transverse section of the carotid bulb acquired by CT scan in PAS1. (b, c) Three-dimensional reconstruction of the arterial structure displayed from two viewing angles. The calcification (CA), residual lumen (L), fibrous atheromatous tissue (FT) and stenosis position (ST) are identified. Note that these CT scan 3-D reconstructions support the interpretation of our elastograms.

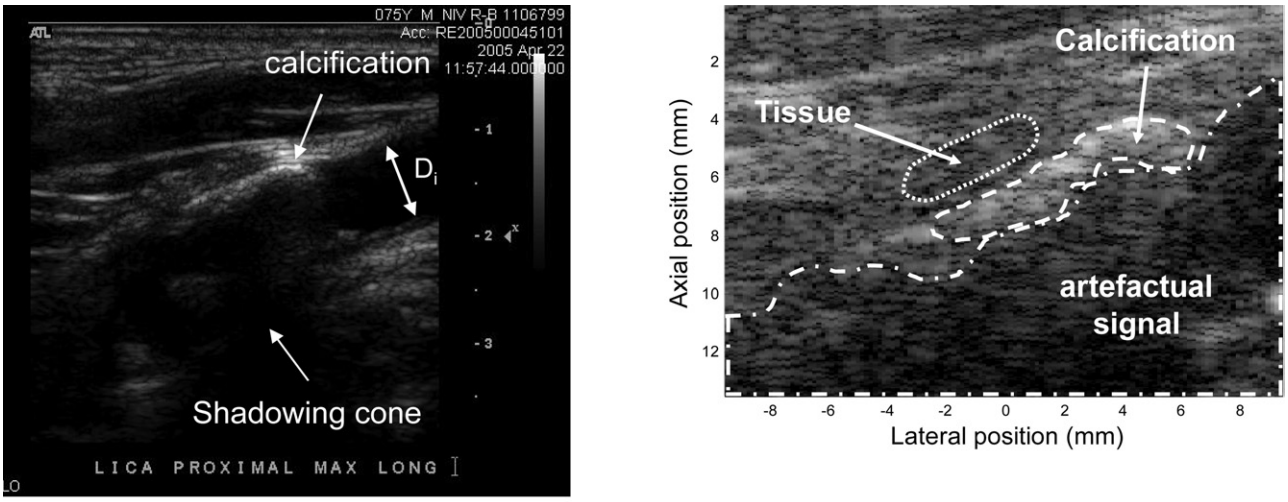

Fig. 10. (a) Longitudinal B-mode image of a 75-year-old pathologic male's proximal internal carotid artery acquired with the Philips 5000 US clinical scanner and (b) the research acquisition system Ultrasonix RP550. The calcification, shadowing cone, normal lumen inner diameter (D_i), reference tissue and artefactual signal are defined.

which appeared to be hyperechogenic; and reference tissue (RT) and presumably normal (NT), localized behind or beside the CP.

Parameter selection in postprocessing

The LSME algorithm was implemented with the parameters (up-sampling rate, window size and window overlap) given in Table 1. Choices were made according to previous numerical simulations, *in vitro* phantom studies (Schmitt 2005) and images presented in this article. They depend mainly on image quality (signal-to-noise ratio [SNR], patient breathing, artefactual tissue motion, *etc.*). In healthy subjects, a high SNR and a homogenous arterial wall mechanical configuration allowed us to apply large window sizes. However, RF images from heterogenous wall acquisitions of patients limited window size because of the need to find small heterogeneities (calcification deposits, soft plaque, *etc.*). Bi-cubic up-sampling interpolation increased the estimation resolution in images of pathologic subjects.

RESULTS

Healthy subjects

Compared with older people, the carotid artery wall of young, healthy subjects differs in numerous characteristics: homogenous wall composition, good SNR of US images and high elasticity. Thus, we decided to first study the mechanical properties of the right common distal carotid artery of a 26-year-old healthy male to validate our method under optimal conditions, then present the result of a 40-year-old healthy woman. The investigation of longitudinal images was chosen because of the unidirectionality of vessel motion (perpendicular to blood flow).

B-mode images, calculated from a log-compressed version of the RF signal envelope, are presented in Figs. 3 and 6. The lumen, proximal and distal walls could easily be segmented for HS1, whereas only the inferior wall was analyzed for HS2 because of low US quality. Axial strain (ε_{yy}) distribution was assessed between pairs of consecutive RF images. Cumulative elastograms for each cardiac cycle were then calculated. An average from all cycles was determined, and mean axial strain in a small window (0.38×1.19 mm centered at $x = 0$ mm for HS1 and $x = 5$ for HS2), depicted in Fig. 3 (RI_1) and Fig. 6 (RI_3), was plotted as a function of time (Figs. 4a and 7a). Knowing the systolic and diastolic pressures, these plots were used to estimate the instantaneous pressure used to solve the inverse problem (stress-strain relationship) defined in eqn (16). Stress-strain modulus distribution was reconstructed at peak-systole and for the diastolic phase.

Axial strain ε_{yy} calculated for instants ① and ②, are shown in Figs. 4b and 7b. For visual comparison, a similar scale (between 0 to 7% for Fig. 4 and 0 to 8% for Fig. 7) was adapted. Corresponding stress-strain modulus maps are presented in Fig. 4c (with a scale going from 0–540 kPa) and 7c (with a scale going from 0–800 kPa). As can be seen in Fig. 4b, proximal wall deformation was smaller than the distal one. According to the $E_{stress\text{-}strain}$ maps, the proximal wall was indeed less elastic (higher moduli). Within a large region defined in

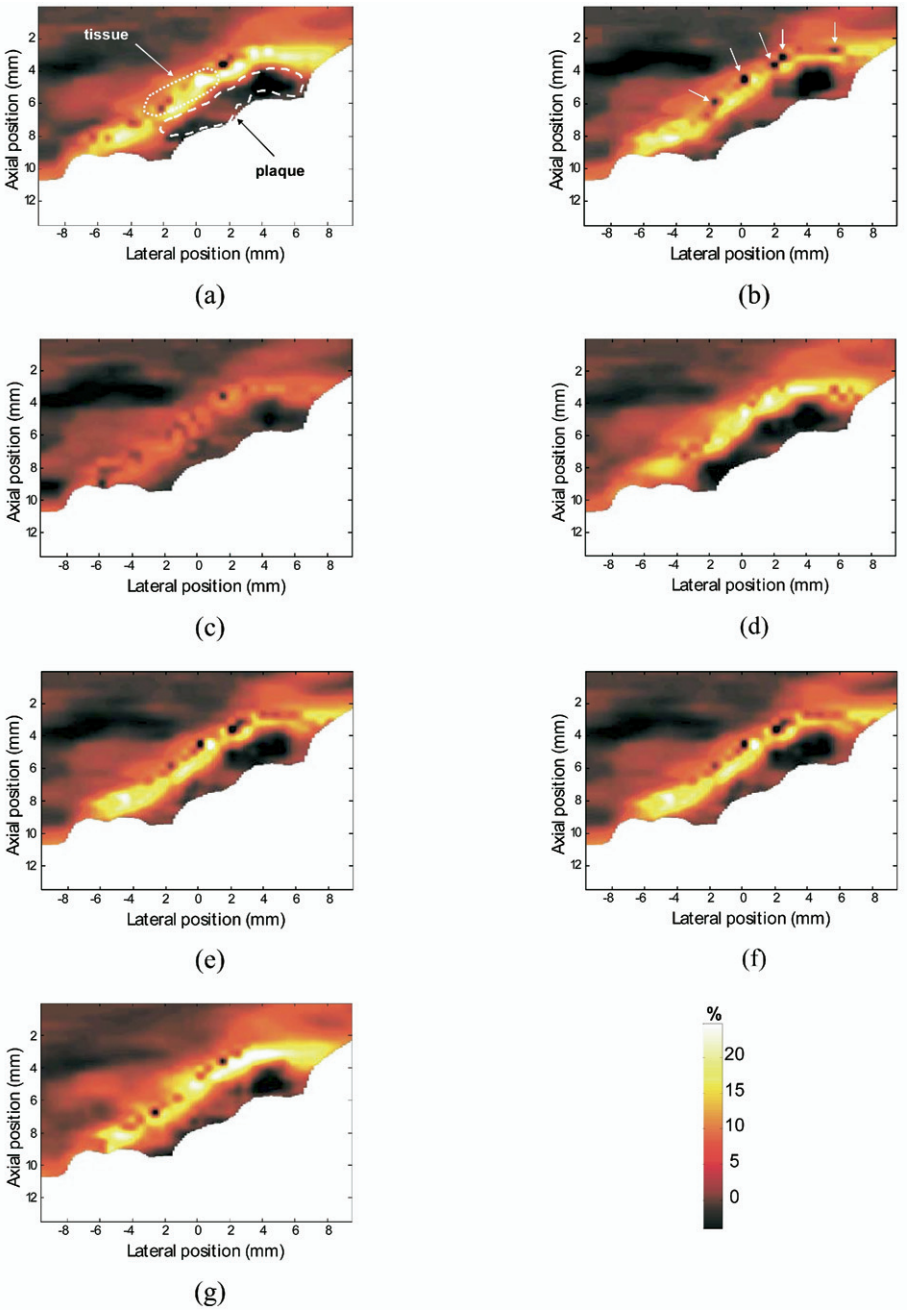

Fig. 11. Cumulated axial strain distribution between end-diastole and peak-systole for seven consecutive cardiac cycles. The cardiac cycles are represented from the first (top panel) to the seventh (bottom panel) cycle. The color scale ranges from −4% to 25%. The plaque and reference tissue are segmented on the first elastogram. Local estimation errors are indicated with white arrows on the second elastogram. The lumen is segmented in white.

the inferior wall (RI_2 in Fig. 4c and RI_4 in Fig. 7c), the $E_{stress\text{-}strain}$ dispersion was 199 ± 12 kPa (①) and 213 ± 14 kPa (②) for HS1, and 434 ± 211 kPa (①) and 682 ± 235 kPa (②) for HS2.

Finally, vessel mechanical properties were quantitatively characterized by E_{max} (modulus with the highest occurrence) and $DIST_E$ (elasticity homogeneity) over the whole distal wall (Figs. 5 and 8). Mean coefficients of variation over five cardiac cycles, calculated as standard deviations divided by the means, were 8.4% (E_{max}) and

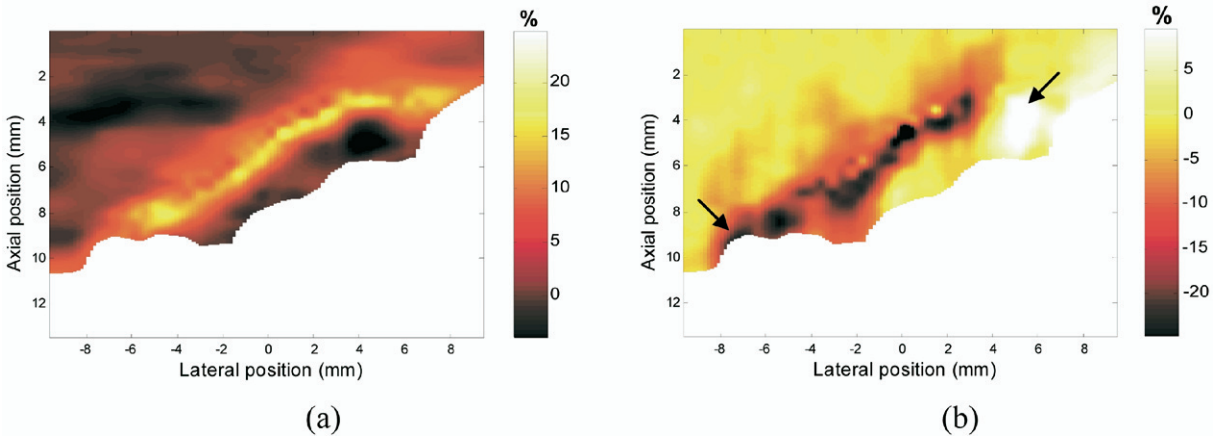

Fig. 12. (a) Axial strain and (b) axial shear averaged on seven consecutive cardiac cycles estimated from longitudinal RF sequences acquired from the proximal left internal carotid artery at the maximal stenosis position. The color scale ranges between (a) –4% and 25% and (b) –25% and 10%. The lumen appears in white.

29.7% ($DIST_E$) for HS1, and 32% (E_{max}) and 52% ($DIST_E$) for HS2. Plot discontinuities coincided with the parietal stress inflexion point in Figs. 4a and 7a (between ② and ①), which was a result of the carotid reflection wave.

Pathologic subjects

The first patient (PAS1) enrolled in this study had developed a large, calcified ring around the left proximal internal carotid artery, whereas PAS2 had calcification deposits on the left distal internal carotid wall. The calcium deposit for PAS1 is displayed in Fig. 9 on the 3-D CT scan (white structures, calcification [CA], in different views). Two-dimensional cross-section images (Fig. 9a) showed an annular calcification surrounding fibrous atheromatous tissue (FT) in the left internal carotid artery and smaller calcified plaque in the right internal carotid and residual lumen (L). Stenosis severity and calcification localization were characterized from 3-D reconstructed images (Fig. 9b and c). Unfortunately, the tissue composition of the plaque jeopardized the quality of the US scans. Indeed, calcification (strong US attenuation) reduced the SNR for regions behind this material.

Longitudinal and cross-sectional acquisitions for PAS1. B-mode images (Fig. 10a) and color Doppler duplex (Fig. 14a) helped to segment the reconstructed B-mode display obtained from the RF data (Figs. 10b and 14b). It should be noted that images in Figs. 10a and 14a compared with Figs. 10b and 14b had different positions and window sizes because of the different US systems and probes employed. During atherosclerosis evolution, the arterial wall is subjected to significant mechanical and morphologic changes. Because of this phenomenon, it is often difficult to identify the healthy portion of the wall on B-mode images. Consequently, it became relevant for us to compare three regions defined arbitrarily as (Figs. 10b and 14b): the calcification (CA), the reference tissue (RT, conventionally, we used *tissue* as the material localized around the vessel or in the presumably healthy section of the arterial wall that showed much less stiffness than the plaque) and the artefactual signal. This last region, according to Fig. 9a, included fibrous plaque and the lumen, but the shadowing artefact induced by a significant calcified zone did not allow us to differentiate them. Disease-free common carotid inner diameter (D_i) was 7.25 mm. Radiofrequency image sequences of 7.5 s were acquired, representing seven entire cardiac cycles. Cumulated elastograms from end-diastole to peak-systole are shown in

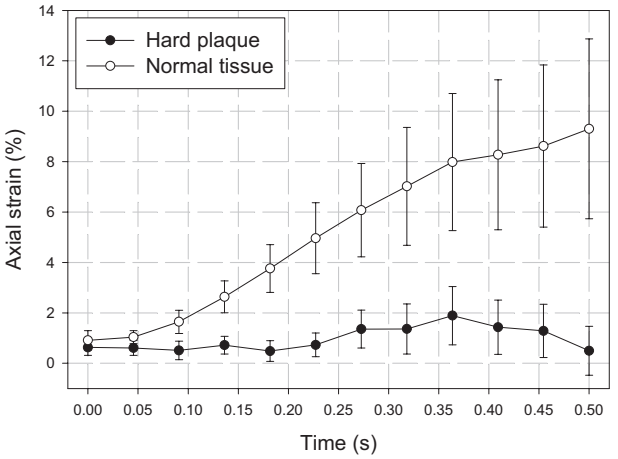

Fig. 13. Mean and standard deviation of axial strain within corresponding defined whole regions averaged on seven cardiac cycles between end-diastole (t = 0 s) and peak-systole (t = 0.5 s).

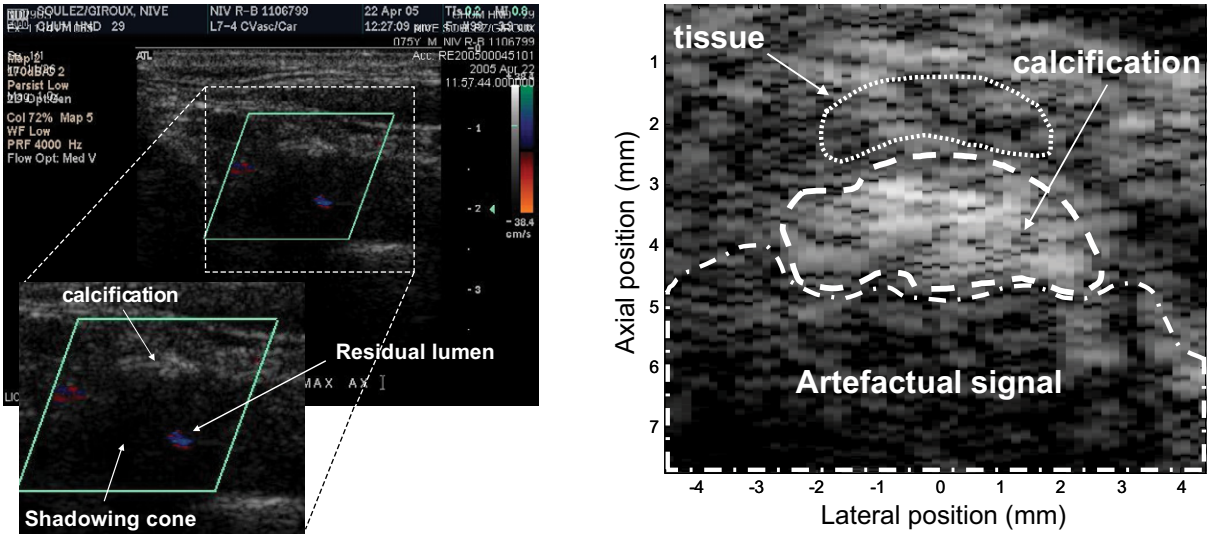

Fig. 14. (a) Longitudinal color-Doppler image of the left proximal internal carotid artery acquired with the Philips 5000 ultrasound system and (b) B-mode image of the same carotid acquired with the Ultrasonix RP550 scanner. The calcification, shadowing cone, residual lumen, reference tissue and artefactual signal are highlighted on both images.

Figs. 11 and 15 for each cardiac cycle (from the first at the top left, to the seventh at the bottom left). The color bar ranges from –4 to 25%. From longitudinal acquisitions, assessed elastograms describe similar characteristics for the different cardiac cycles: a low deformable structure in the plaque area corresponding to CA (between –4% and 5%), a more deformable structure above it corresponding to the presumably healthy section of the vessel (between 10 and 25%), and a structure corresponding to the adventitia with medium deformations (between 5 and 10%). Cross-sectional strain distributions can be presented as a hard structure (low strain between –2 and 5%) in the lower part of each panel, whereas a deformable, ring-shaped region (high strain from 5–16%) spreads from the left to the right. Strain regularity and continuity in the soft ring denotes homogenous material mechanical properties. Arterial wall dynamic behavior was different compared with the longitudinal view that displayed strain mainly in the axial direction, but deformation values were of the same order. Axial strain distributions also gave some estimation errors identified by white arrows in Figs. 11b and 15d. These artefacts have different locations according to the cycle.

By averaging the seven elastograms of Figs. 11 and 15, local estimation errors are removed, and plaque contrast is increased (Figs. 12a and 16a). Study of axial shear adds pertinent information about mechanical interactions between structures (Figs. 12b and 16b). Shear distribution in longitudinal scans is mapped as a heterogenous pattern. As indicated by the left arrow, this distribution is characterized by opposite shear values between the bottom left section of the plaque (~6%) and its left superior extremity (about –14%). The right arrow indicates the other site of opposite shear components. From cross-sectional acquisition, axial shear image showing central symmetry is characterized by the highest axial shear values localized at the border between soft and hard structures (about –20% at $x = -4$ mm and $y = 4$ mm; ~26% at $x = 3$ mm and $y = 4$ mm).

From 2-D elastograms, quantitative investigations were undertaken to study the dynamic behavior of plaque and surrounding tissue. Instantaneous means and standard deviations of axial strain for seven consecutive cardiac cycles in early systole are plotted in Figs. 13 and 17 for presumably healthy tissue and calcified plaque identified in Figs. 10b and 14b. This information clearly allows us to discriminate two regions with different mechanical properties (mean elasticity ratios between 0 and 0.5 s equal to 5.8 ± 4.5 and 7.2 ± 2.7 for longitudinal and cross-sectional scans, respectively).

Longitudinal acquisition for PAS2. Radiofrequency image sequences were acquired on the left distal internal carotid artery. The investigated region is displayed as a B-mode image in Fig. 18a. We restricted mechanical parameter estimation to the small region defined by the white window in the dotted line, which includes the calcification deposit (bright echogenic plaque) and a presumably normal wall section (Fig. 18b). Radiofrequency image acquisition represented four entire cardiac cycles. Cumulated axial strain in early systole (from end-diastole to peak-systole) is illustrated in Fig. 19a-d

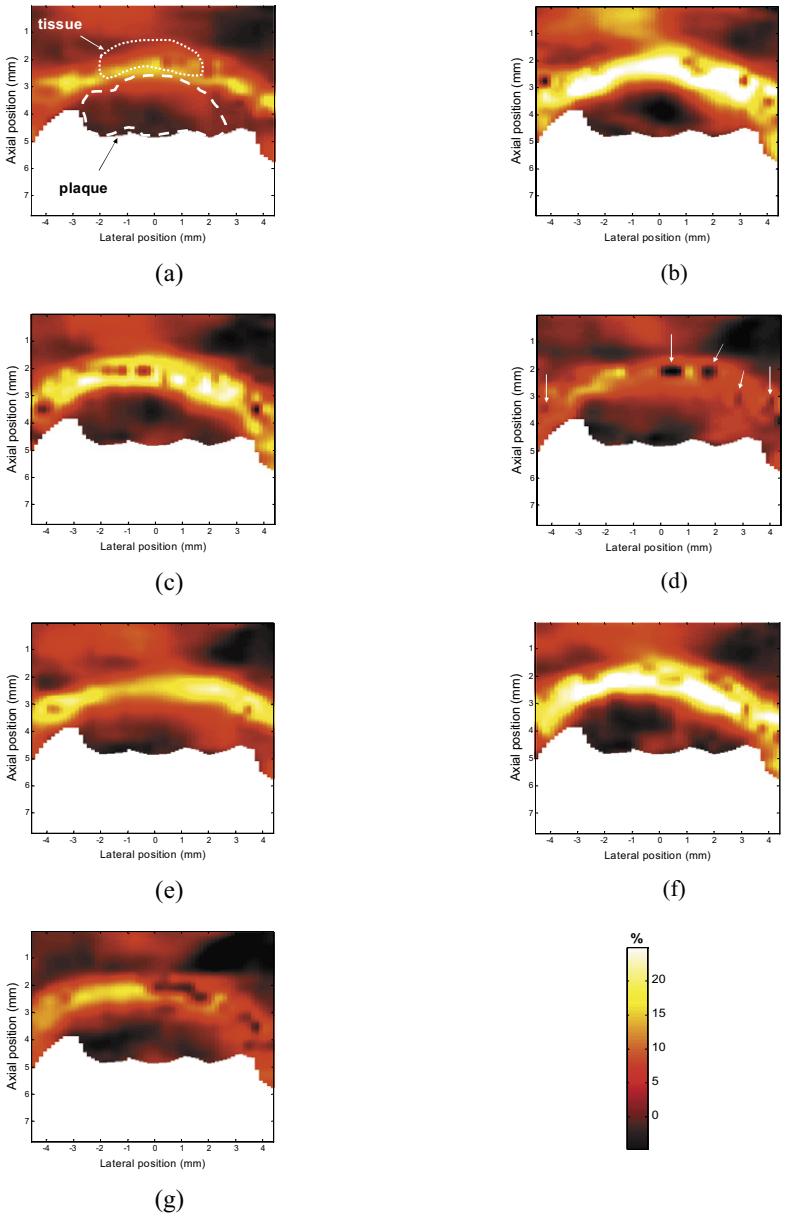

Fig. 15. Cumulated axial strain distribution between end-diastole and peak-systole for seven consecutive cardiac cycles. The cardiac cycles are represented from the first (top panel) to the seventh (bottom panel) cycle. The color scale ranges from –5% to 25%. The plaque and reference tissue are segmented on the first elastogram. Local estimation errors are indicated with white arrows on the fourth elastogram. The lumen appears in white.

for each cardiac cycle. Elastogram quality improvement in terms of contrast and local mis-estimation correction was obtained by averaging the cumulated elastograms over four cycles (Fig. 19e). All elastograms were plotted with the same color bar ranging from 0 to 10%, with the lumen being segmented manually and displayed in white. According to Fig. 19e, axial strain varied between about –1 to 3% and between ~5 to 7% for the hard plaque and normal tissue, respectively.

Because the RF signals had a high SNR for this patient, the time-varying mechanical behavior of the wall was studied over the whole cardiac cycle. Figure 20 was built by cumulating strains from end-diastole. Mechanical contrast between the plaque and normal tissue was

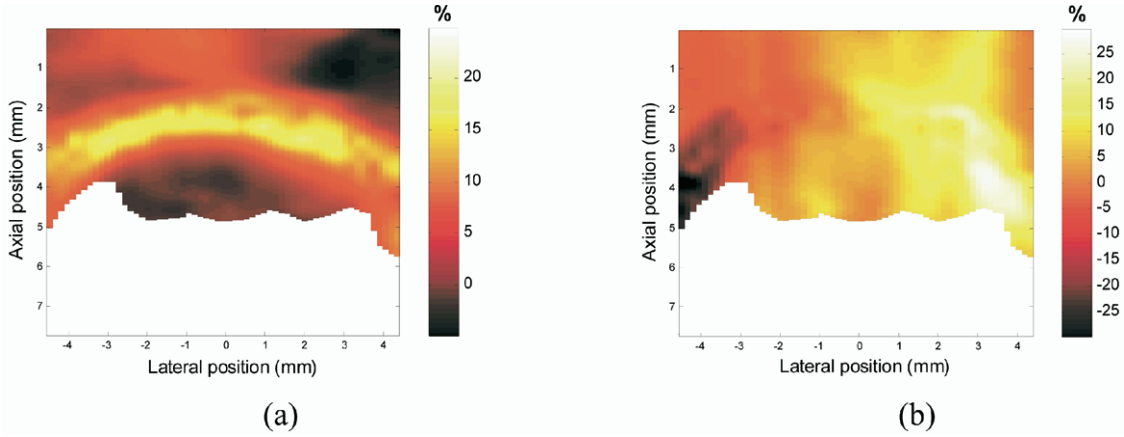

Fig. 16. (a) Axial strain and (b) axial shear averaged on seven consecutive cardiac cycles estimated from axial RF sequences acquired from the proximal left internal carotid artery at the maximal stenosis position. The color scale ranges between (a) –5% and 25% and (b) –30% and 30%. The lumen is segmented in white.

evaluated quantitatively as a mean elasticity ratio between 0 and 1.2 s of 2.8 ± 1.6.

DISCUSSION

Healthy subjects

Elastogram estimation. Noninvasive vascular elastography aims to reconstruct and evaluate arterial wall absolute elasticity. However, it is crucial to assess reliable and stable elastograms to solve inverse problems. In the framework of noninvasive applications, the calculation of cumulated elastograms obtained for small successive deformations enhanced the elastograms' SNR (Varghese and Ophir 1996). Moreover, for most proposed methods found in the literature, strain is calculated from the gradient of assessed displacement fields. The differentiator operator has a high sensitivity to local errors, which implies the need for displacement fields of good quality. The method proposed here directly estimates the strain tensor, which should be an improvement over other existing approaches.

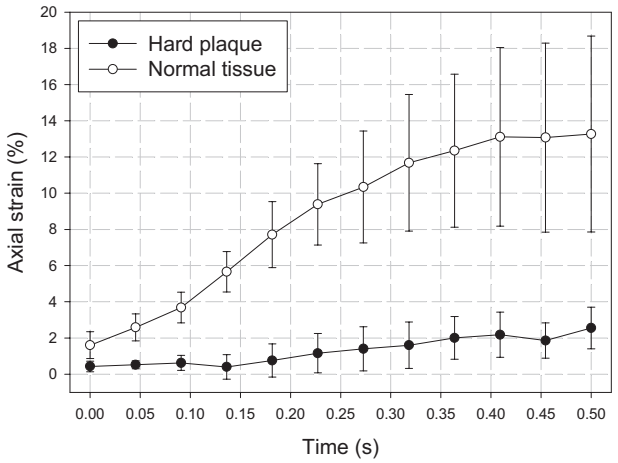

Fig. 17. Mean and standard deviation of axial strain within corresponding defined whole regions averaged on seven cardiac cycles between end-diastole (t = 0 s) and peak-systole (t = 0.5 s).

Axial strain reproducibility and local axial strain profile. The stress-strain elasticity modulus assessed for HS1 (a 26-year-old healthy man) was reproducible, at least on five consecutive cardiac cycles with an acceptable coefficient of variation at peak-systole of 4.7%. In Hasegawa et al. (1998), the normalized standard deviation average was around 3% for three consecutive cardiac cycles for a population of 54 subjects in the range of 32 to 66 years old. Although too premature to draw a conclusion, our method also seems reproducible. Interestingly, time-varying axial strain in Figs. 4a and 7a allowed us to characterize the timing of the reflection wave added to the forward wave. These results in Figs. 4a and 7a are comparable to the pressure waveforms found in the literature (Izzo and Shykoff 2001).

Inverse problem and proposed mechanical parameters. For clinical application, assessment of robust absolute mechanical parameters would overcome numerous problems of interpretation. In the case of simple geometries (axisymmetric and isotropic vessel walls), we proposed an inverse problem to calculate the stress-strain elastic modulus. As introduced by Kanai et al. (2003), histograms were used to present elasticity distributions. They suggested the calculation of mean and standard deviation values within ROI. However, in the cases presented by Kanai et al. (2003), distributions were not described by a symmetrical law (*i.e.*, Gaussian). As a consequence, the mean values do not present elasticity with the highest occurrence. In practice, two tissues with

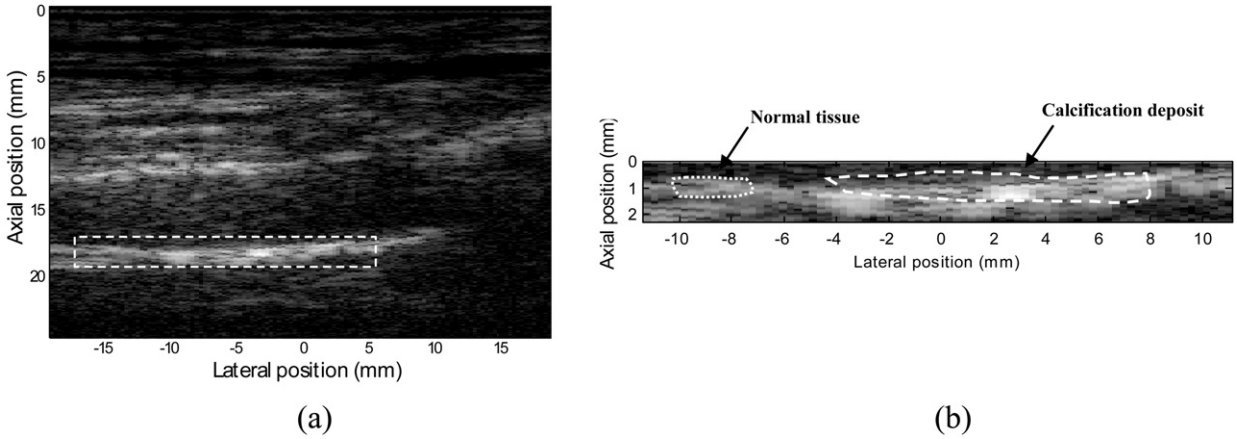

Fig. 18. (a) Longitudinal B-mode image of a 75-year-old pathologic male's left distal internal carotid artery. (b) On the proximal wall, a calcification deposit and normal tissue regions are defined.

the same elasticity, but with different elasticity dispersions, need to be discriminated. We introduced E_{max} and $DIST_E$ as robust parameters likely to resolve this type of ambiguity.

Proximal wall vs. *distal wall analysis.* Golemati et al. (2003) studied the dynamics of healthy common carotid arterial walls to demonstrate higher-amplitude motion for the posterior than for the anterior wall. They noted that the posterior wall has a higher deformation. Our results in Fig. 4b allow us not only to validate this phenomenon, but also to calculate a strain ratio of 2.5 between the two walls. Golemati et al. (2003) explained this dynamic difference by the lower-quality B-mode images of the proximal wall. Other factors to consider may be the effect of applied probe pressure on the skin during scanning and the impact of surrounding tissue heterogeneity. Indeed, the presence of rigid structures (*i.e.*, bone) modifies the stress pattern distribution in the medium.

Subjects with carotid plaques

Importance of calcification detection. Large calcified areas identified in the carotid artery wall of both patients are of prognostic value for plaque mechanical stability. Indeed, numerous studies have demonstrated that plaque composition is a better predictor of stroke than stenosis severity. The presence of calcium, in the majority of atherosclerotic arteries, is considered to stabilize the plaque and protect against plaque rupture (Fisher et al. 2005; Huang et al. 2001; Nandalur et al. 2005; Shaalan et al. 2004). Nevertheless, there are some ambiguities about the utility of calcification characterization as a possible parameter discriminating between symptomatic and asymptomatic patients. Although the current study did not compare the accuracy of B-mode and strain mode imaging to detect calcium, our results in Figs. 12, 16 and 19 detect and quantify the impact of calcium deposits on wall mechanical behavior (low strain).

Estimation reproducibility of heterogenous walls. Cross-sectional and longitudinal estimations of strain and shear gave acceptable intercycle reproducibility despite RF image quality degradation as a result of calcification and complex artefactual motions (*i.e.*, breathing, probe motion, *etc.*). Some differences were nevertheless noted between cycles. Golemati et al. (2003) and Bang et al. (2003) published their results on carotid motion estimation. Axial and lateral wall motions as a function of time showed periodicity, but the static (maximal, minimal and mean values) and dynamic (increasing and decreasing slopes) characteristics were not reproducible on two consecutive cycles. The study by Dahl et al. (2004) confirmed the effect of complex wall motion on artery dynamics because only four among 29 parameters (*i.e.*, horizontal and vertical displacements, *etc.*) produced reproducible measurements in the systolic phase. According to our results, strain and shear measurements may be more reproducible than motion estimators.

Comparison of reference tissues with plaque regions. Mean strain values within arbitrarily selected tissue and plaque regions clearly indicated two different time-varying mechanical characteristics. Axial strain ratios quantitatively distinguished area composition on cross-sectional (7.2 ± 2.7 for PP1) and longitudinal (5.8 ± 4.5 for PP1, 2.8 ± 1.6 for PP2) acquisitions. If we compare the results for PP1, the ratio difference was likely because of plaque thickness. Indeed, strain was inversely dependent on plaque thickness. Cross-sectional acquisitions were located in the region of maximal stenosis, which implied thicker plaque and relatively lower mean strain.

Two hypotheses may explain the presence of a 2-mm soft layer with cumulative strains in the order of 15 to 20%

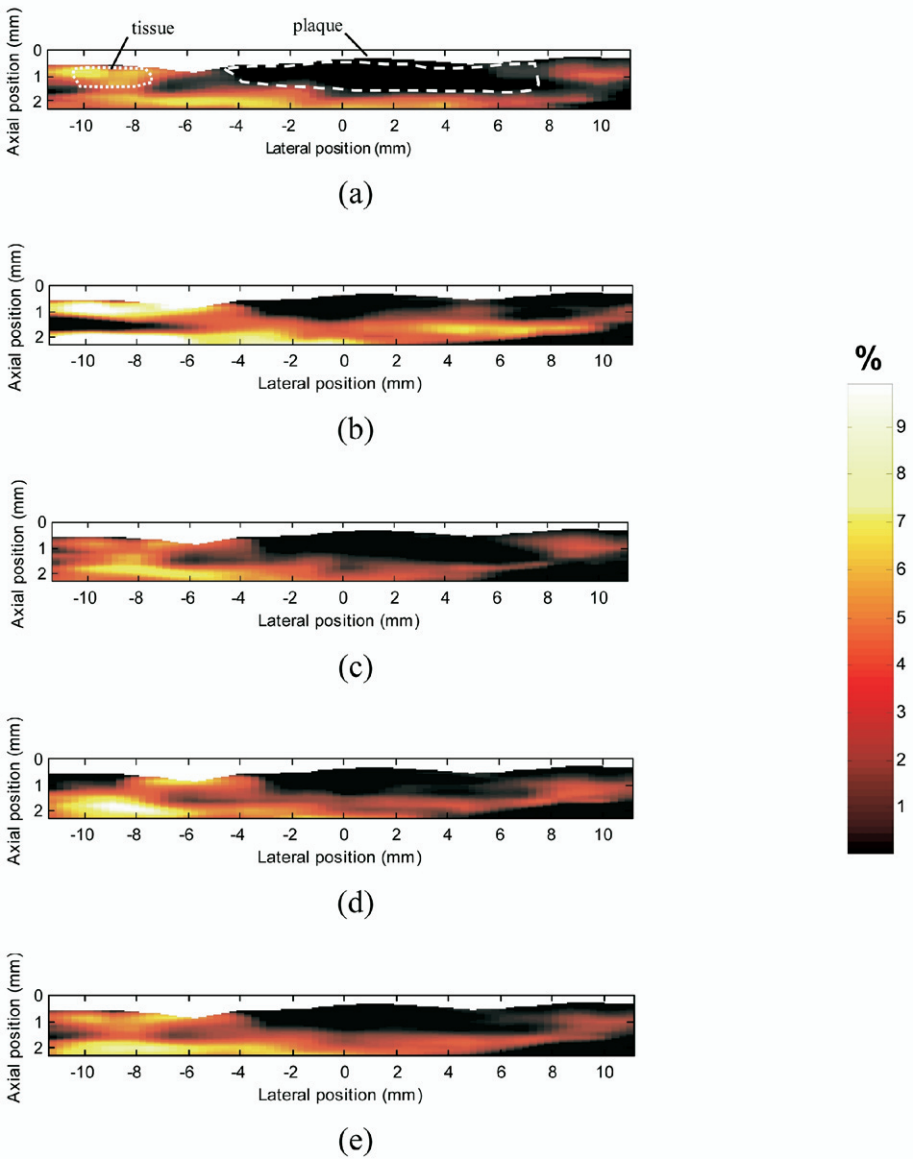

Fig. 19. (a, b, c, d) Cumulated axial strain distribution between end-diastole and peak-systole for four consecutive cardiac cycles. The cardiac cycles are represented for the first (a) to the fourth (d) cycle. The plaque and reference tissue are segmented on the first elastogram. (e) Axial strain averaged on four consecutive cardiac cycles estimated from longitudinal RF sequences. The color scale ranges from 0% to 10%. The lumen is segmented in white.

in Fig. 15. First, the very hard calcified plaque close to the vessel lumen induced mechanical stress repartition with the transfer of high energy to the surrounding tissue, which induced a large cumulated deformation. Second, the perivascular region is made up of compliant fat. The selected tissue area includes probably adventitial tissue and perivascular fat.

It was noted that axial strain distributions presented local errors of estimation and negative values. The origin of the first artefact may be linked to RF image quality (low SNR for some scans), to the robustness of our estimator, and to the assumption underlying our model (constant motion in a ROI). Moreover, limited ROI size and data sensitivity may produce divergence of the iterative process of the LSME implanted version, described in the current study. The second artefact (negative strains) is probably a result of the limitation of the algorithm to assess very small deformations. Because the tissue in a hard plaque has mainly displacement motion with very low deformation, axial strain is difficult to track with good accuracy in these circumstances.

Axial shear estimations. Axial shear is a relevant parameter to understand the mechanical behavior of in-

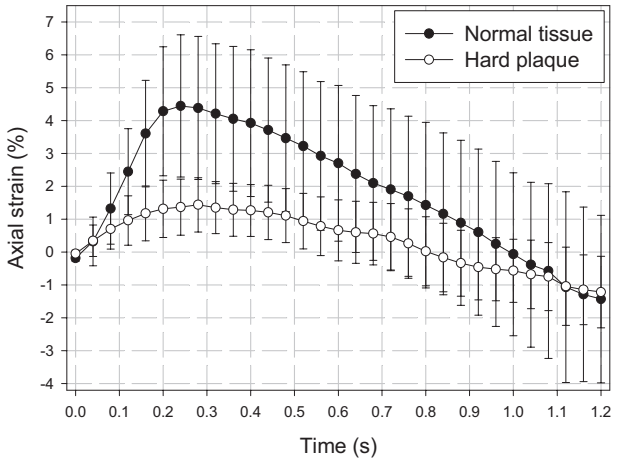

Fig. 20. Means and standard deviations of axial strain within corresponding defined whole regions averaged on four cardiac cycles in an entire cycle (between $t = 0$ s to $t = 1.2$ s).

terfaces between two regions. Indeed, hard structure mobility (*i.e.*, rotation) is relevant information to know more about interactions with surrounding tissues. Our method assessed maximal shear in regions close to the lumen and at the interface between hard and soft materials. These results are in good agreement with mechanical simulations investigated with similar plaque compositions (Maurice et al. 2004). Moreover, we observed shear repartition along hard plaque in longitudinal acquisitions. This shear pattern is generated by lateral wall motion as a result of pressure wave propagation (Golemati et al. 2003). The reproducibility validation of axial strain is also equivalent for shear estimates (results not shown). Finally, high shear values may suppose a high risk of inflammation and intraplaque hemorrhage, leading to decreased mechanical plaque stability.

CONCLUSION

A motion estimator adapted for NIVE was formulated to assess axial strain and shear. Because this model takes echo intensity variations into account, it was able to counteract possible decorrelation noise between RF images. The elasticity of healthy common carotid arteries was determined with an appropriate inverse problem by using estimated axial strains. Calculated stress-strain moduli (E_{max}) were in the range of values found by Kanai et al. (2003).

In vivo axial strain and shear distributions of atherosclerotic carotid arteries were presented for the first time. Studies of mechanical interactions between calcification, surrounding tissues and the normal wall are very relevant. Indeed, a controversial issue in the literature is the presence of calcification as a criterion to identify plaques at risk of rupture (Huang et al. 2001; Shaalan et al. 2004; Nandalur et al. 2005). This preliminary study demonstrated the capacity of the method to identify tissue structures with different mechanical properties. Strain and shear distributions may be informative for high stress concentration, which is a good indicator of risk. This estimator is promising for *in vivo* applications aimed at noninvasively characterizing plaque evolution in carotid arteries.

Acknowledgements—Financial support for this research was initially provided by Valorisation-Recherche Québec (group grant #2200-094) and by the Natural Sciences and Engineering Research Council of Canada (grant #138570-01). The project is now funded by the Canadian Institutes of Health Research (grant #PPP-78763) and by Univalor (the Université de Montréal Technology Transfer Office). Dr. Cloutier is the recipient of a National Scientist award, Dr. Soulez of a Clinical Scientist award and Dr. Maurice of a Research Scholarship award from the Fonds de la recherche en santé du Québec (FRSQ). The authors thank Dr. J.-L. Gennisson and Dr. J. Fromageau for some illuminating discussions. The editorial assistance of Dr. Ovid Da Silva, Research Support Office, CHUM Research Centre, is acknowledged.

REFERENCES

Bang J, Dahl T, Bruinsma A, Kaspersen JH, Hernes TAN, Myhre HO. A new method for analysis of motion of carotid plaques from RF ultrasound images. Ultrasound Med Biol 2003;29:967–976.

Casscells W, Naghavi M, Willerson JT. Vulnerable atherosclerotic plaque: A multifocal disease. Circulation 2003;107:2072–2075.

Chaturvedi S. Public health impact of carotid endarterectomy. Neuroepidemiology 1999;18:15–21.

Connors JJ, Seidenwurm D, Wojak JC, Hurst RW, Jensen ME, Wallace R, Tomsick T, Barr J, Kerber C, Russell E, Nesbit GM, Fox AJ, Tsai FY. Treatment of atherosclerotic disease at the cervical carotid bifurcation: Current status and review of the literature. AJNR Am J Neuroradiology 2000;21:444–450.

Dahl T, Bang J, Ushakova A, Lydersen S, Myhre HO. Parameters describing motion in carotid artery plaques from ultrasound examination: A reproducibility study. Ultrasound Med Biol 2004;30:1133–1143.

ECST. Randomised trial of endarterectomy for recently symptomatic carotid stenosis: Final results of the MRC European Carotid Surgery Trial. Lancet 1998;351:1379–1387.

Faxon DP, Fuster V, Libby P, Beckman JA, Hiatt WR, Thompson RW, Topper JN, Annex BH, Rundback JH, Fabunmi RP, Robertson RM, Loscalzo J. Atherosclerotic Vascular Disease Conference: Writing Group III: Pathophysiology. Circulation 2004;109:2617–2625.

Fisher M, Paganini-Hill A, Martin A, Cosgrove M, Toole JF, Barnett HJM, Norris J. Carotid plaque pathology—Thrombosis, ulceration, and stroke pathogenesis. Stroke 2005;36:253–257.

Golemati S, Sassano A, Lever MJ, Bharath AA, Dhanjil S, Nicolaides AN. Carotid artery wall motion estimated from B-mode ultrasound using region tracking and block matching. Ultrasound Med Biol 2003;29:387–399.

Hasegawa H, Kanai H, Hoshimiya N, Chubachi N, Koiwa Y. Measurement of local elasticity of human carotid arterial walls and its relationship with risk index of atherosclerosis. IEEE Ultrason Symp 1998;2:1454–1457.

Huang H, Virmani R, Younis H, Burke AP, Kamm RD, Lee RT. The impact of calcification on the biomechanical stability of atherosclerotic plaques. Circulation 2001;103:1051–1056.

Imparato AM, Riles TS, Mintzer R, Baumann FG. The importance of hemorrhage in the relationship between gross morphologic characteristics and cerebral symptoms in 376 carotid artery plaques. Ann Surg 1983;197:195–203.

Izzo JL Jr, Shykoff BE. Arterial stiffness: Clinical relevance, measurement, and treatment. Rev Cardiovasc Med 2001;2:29–40.

Kanai H, Hasegawa H, Ichiki M, Tezuka F, Koiwa Y. Elasticity imaging of atheroma with transcutaneous ultrasound: Preliminary study. Circulation 2003;107:3018–3021.

Kazmierski R, Watala C, Lukasik M, Kozubski W. Common carotid artery remodeling studied by sonomorphological criteria. J Neuroimaging 2004;14:258–264.

Kolodgie FD, Gold HK, Burke AP, Fowler DR, Kruth HS, Weber DK, Farb A, Guerrero LJ, Hayase M, Kutys R, Narula J, Finn AV, Virmani R. Intraplaque hemorrhage and progression of coronary atheroma. N Engl J Med 2003;349:2316–2325.

Langeland S, D'hooge J, Torp H, Bijnens B, Suetens P. Comparison of time-domain displacement estimators for two-dimensional rf tracking. Ultrasound Med Biol 2003;29:1177–1186.

Lehmann ED. Terminology for the definition of arterial elastic properties. Pathol Biol (Paris) 1999;47:656–664.

Maurice RL, Bertrand M. Speckle-motion artifact under tissue shearing. IEEE Transact Ultrason Ferroelect Freq Control 1999;48:584–594.

Maurice RL, Ohayon J, Fretigny Y, Bertrand M, Soulez G, Cloutier G. Noninvasive vascular elastography: Theoretical framework. IEEE Transact Med Imaging 2004;23:164–180.

Meairs S, Hennerici M. Four-dimensional ultrasonographic characterization of plaque surface motion in patients with symptomatic and asymptomatic carotid artery stenosis. Stroke 1999;30:1807–1813.

Montauban van Swijndregt AD, Elbers HR, Moll FL, de Letter J, Ackerstaff RG. Cerebral ischemic disease and morphometric analyses of carotid plaques. Ann Vasc Surg 1999;13:468–474.

Naghavi M, Libby P, Falk E, Casscells SW, Litovsky S, Rumberger J, Badimon JJ, Stefanadis C, Moreno P, Pasterkamp G, Fayad Z, Stone PH, Waxman S, Raggi P, Madjid M, et al. From vulnerable plaque to vulnerable patient—A call for new definitions and risk assessment strategies: Part I. Circulation 2003;108:1664–1672.

Nandalur KR, Baskurt R, Hagspiel KD, Phillips CD, Kramer CM. Calcified carotid atherosclerotic plaque is associated less with ischemic symptoms than is noncalcified plaque on MDCT. AJR Am J Roentgenology 2005;184:295–298.

NASCET. Beneficial effect of carotid endarterectomy in symptomatic patients with high-grade carotid stenosis. North American Symptomatic Carotid Endarterectomy Trial Collaborators. N Engl J Med 1991;325:445–453.

Nicolaides A, Sabetai M, Kakkos SK, Dhanjil S, Tegos T, Stevens JM, Thomas DJ, Francis S, Griffin M, Geroulakos G, Ioannidou E, Kyriacou E. The Asymptomatic Carotid Stenosis and Risk of Stroke (ACSRS) Study. Aims and results of quality control. Int Angiol 2003;22:263–272.

O'Rourke MF, Staessen JA, Vlachopoulos C, Duprez D, Plante GE. Clinical applications of arterial stiffness: Definitions and reference values. Am J Hypertens 2002;15:426–444.

Periaswamy S, Farid H. Elastic registration in the presence of intensity variations. IEEE Transact Med Imaging 2003;22:865–874.

Reneman RS, Meinders JM, Hoeks APG. Non-invasive ultrasound in arterial wall dynamics in humans: What have we learned and what remains to be solved. Eur Heart J 2005;26:960–966.

Schmitt C. Non invasive vascular elastography: Toward a complementary characterization tool of atherosclerosis in carotid arteries, M.Sc. dissertation, University of Montreal, 2005.

Segers P, Rabben SI, De Backer J, De Sutter J, Gillebert TC, Van Bortel L, Verdonck P. Functional analysis of the common carotid artery: Relative distension differences over the vessel wall measured in vivo. J Hypertens 2004;22:973–981.

Shaalan WE, Cheng HW, Gewertz B, McKinsey JF, Schwartz LB, Katz D, Cao DC, Desai T, Glagov S, Bassiouny HS. Degree of carotid plaque calcification in relation to symptomatic outcome and plaque inflammation. J Vasc Surg 2004;40:262–269.

Takaya N, Yuan C, Chu B, Saam T, Polissar NL, Jarvik GP, Isaac C, McDonough J, Natiello C, Small R, Ferguson MS, Hatsukami TS. Presence of intraplaque hemorrhage stimulates progression of carotid atherosclerotic plaques: A high-resolution magnetic resonance imaging study. Circulation 2005;111:2768–2775.

Thom T, Haase N, Rosamond W, Howard VJ, Rumsfeld J, Manolio T, Zheng ZJ, Flegal K, O'Donnell C, Kittner S, Lloyd-Jones D, Goff DC Jr, Hong Y, Adams R, Friday G, et al. Heart disease and stroke statistics—2006 update: A report from the American Heart Association Statistics Committee and Stroke Statistics Subcommittee. Circulation 2006;113:e85–e151.

Varghese T, Ophir J. Performance optimization in elastography: Multicompression with temporal stretching. Ultrason Imaging 1996;18:193–214.

Yeung F, Levinson SF, Parker KJ. Multilevel and motion model-based ultrasonic speckle tracking algorithms. Ultrasound Med Biol 1998;2:427–441.